The Crystallography of Diverse Intermetallic Phases in Binary La-Ni Alloy Obtained by Melting and Its Structural Evolution under High Temperature Sintering

Yibo Liu [1,†], Tenghui Ren[1,†], Bin Wen [1], Zhefeng Xu [1,2], Yuefeng Wang [1], Changzeng Fan [1,2,*] and Lifeng Zhang [1,3,*]

[1] State Key Laboratory of Metastable Materials Science and Technology, Yanshan University, Qinhuangdao 066004, China; 202121020059@stumail.ysu.edu.cn (Y.L.); RTenghui@163.com (T.R.); wenbin@ysu.edu.cn (B.W.); zfxu@ysu.edu.cn (Z.X.); wangyuefeng@ysu.edu.cn (Y.W.)

[2] Hebei Key Lab for Optimizing Metal Product Technology and Performance, Yanshan University, Qinhuangdao 066004, China

[3] School of Mechanical and Materials Engineering, North China University of Technology, Beijing 100144, China

[†] These authors contribute equally.

* Corresponding author. E-mail: chzfan@ysu.edu.cn (C.F.); zhanglifeng@ncut.edu.cn (L.Z.)

Supplementary materials include:

Figure S1. Reciprocal lattice patterns of the La_7Ni_3 phase projected in three axes: (a) *a** axis; (b) *b** axis; (c) *c** axis and its crystal structure projected in *c* axis (d).

Figure S2. Reciprocal lattice patterns of the LaNi phase projected in three axes: (a) *a** axis; (b) *b** axis; (c) *c** axis and its crystal structure projected in *c* axis (d).

Figure S3. Reciprocal lattice patterns of the $LaNi_5$ phase projected in three axes: (a) *a** axis; (b) *b** axis; (c) *c** axis and its crystal structure projected in *c* axis (d).

Figure S4. (a) The Phi360 diffraction pattern collected in the process of single crystal testing, (b) the powder diffraction pattern obtained by integrating the Phi360 diffraction pattern.

Figure S5. Powder diffraction pattern of the remaining 1094 diffraction points (margin).

Figure S6. Reciprocal lattice patterns of the LaNi phase projected in three axes: (a) *a** axis; (b) *b** axis; (c) *c** axis and its crystal structure projected in *c* axis (d).

Figure S7. Reciprocal lattice patterns of the $La_3Ni_3Si_2$ phase projected in three axes: (a) *a** axis; (b) *b** axis; (c) *c** axis and its crystal structure projected in *c* axis (d).

Figure S8. Reciprocal lattice patterns of the La_2NiSi phase projected in three axes: (a) *a** axis; (b) *b** axis; (c) *c** axis and its crystal structure projected in *c* axis (d).

Figure S9. The precession images (a) (0*kl*), (b) (*h*0*l*), (c) (*hk*0) crystal planes of LaNi phase in the SXRD test, LaNi phase simulated diffraction pattern with axes in (d) [100], (e) [010], and (f) [001].

Figure S10. The precession images (a) (0*kl*), (b) (*h*0*l*), (c) (*hk*0) crystal planes of $La_3Ni_3Si_2$ phase in the SXRD test, $La_3Ni_3Si_2$ phase simulated diffraction pattern with axes in (d) [100], (e) [010], and (f) [001].

Figure S11. The precession images (a) (0*kl*), (b) (*h*0*l*), (c) (*hk*0) crystal planes of La_2NiSi phase in the SXRD test, La_2NiSi phase simulated diffraction pattern with axes in (d) [100], (e) [010], and (f) [001].

Figure S12. Scanning electron microscope (SEM) micrographs of single crystal sample. EDX analysis was performed for various locations as indicated in Table S1.

Table S1. The EDX results conducted at every scanning location in Figure S12.

Figure S13. Scanning electron microscope (SEM) micrographs of single crystal sample. EDX analysis was performed for various locations as indicated in Table S2.

Table S2. The EDX results conducted at every scanning location in Figure S13.

Figure S14. The precession images: (a) LaNi (1*kl*), (b) LaNi (*h*1*l*), (c) LaNi (*hk*1), (d) $La_3Ni_3Si_2$ (1*kl*), (e) $La_3Ni_3Si_2$ (*h*1*l*), (f) $La_3Ni_3Si_2$ (*hk*1).

Figure S15. The precession images: (a) LaNi (2*kl*), (b) LaNi (*h*2*l*), (c) LaNi (*hk*2), (d) $La_3Ni_3Si_2$ (2*kl*), (e) $La_3Ni_3Si_2$ (*h*2*l*), (f) $La_3Ni_3Si_2$ (*hk*2).

Figure S16. The precession images: (a) LaNi (3*kl*), (b) LaNi (*h*3*l*), (c) LaNi (*hk*3), (d) $La_3Ni_3Si_2$ (3*kl*), (e) $La_3Ni_3Si_2$ (*h*3*l*), (f) $La_3Ni_3Si_2$ (*hk*3).

Figure S17. The precession images: (a) $La_3Ni_3Si_2$ (1*kl*), (b) $La_3Ni_3Si_2$ (*h*1*l*), (c) $La_3Ni_3Si_2$ (*hk*1), (d) La_2NiSi (1*kl*), (e) La_2NiSi (*h*1*l*), (f) La_2NiSi (*hk*1).

Figure S18. The precession images: (a) $La_3Ni_3Si_2$ (2*kl*), (b) $La_3Ni_3Si_2$ (*h*2*l*), (c) $La_3Ni_3Si_2$ (*hk*2), (d) La_2NiSi (2*kl*), (e) La_2NiSi (*h*2*l*), (f) La_2NiSi (*hk*2).

Figure S19. The precession images: (a) $La_3Ni_3Si_2$ (3*kl*), (b) $La_3Ni_3Si_2$ (*h*3*l*), (c) $La_3Ni_3Si_2$ (*hk*3), (d) La_2NiSi (3*kl*), (e) La_2NiSi (*h*3*l*), (f) La_2NiSi (*hk*3).

Figure S20. (a)La-Ni binary convex hull, (b) La-Ni binary phase diagram

Figure S21. La-Ni-Si ternary phase diagram.

Table S3. Crystallographic and experimental data of $La_3Ni_3Si_2$ phase in another sample.

Table S4. Fractional atomic coordinates and equivalent isotropic displacement parameters ($Å^2$) of $La_3Ni_3Si_2$ phase in another sample.

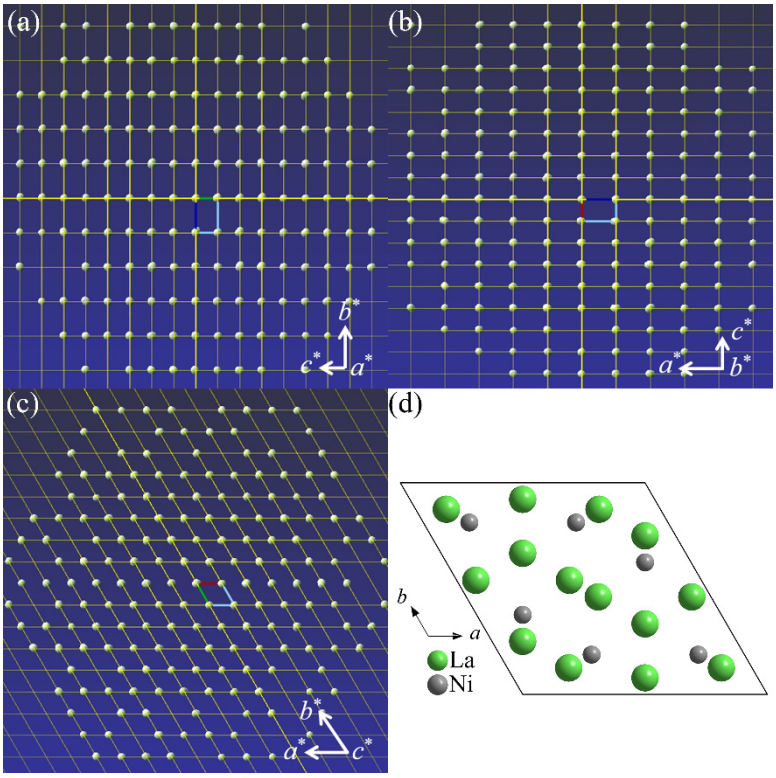

Figure S1. Reciprocal lattice patterns of the La_7Ni_3 phase projected in three axes: (a) *a** axis; (b) *b** axis; (c) *c** axis and its crystal structure projected in *c* axis (d).

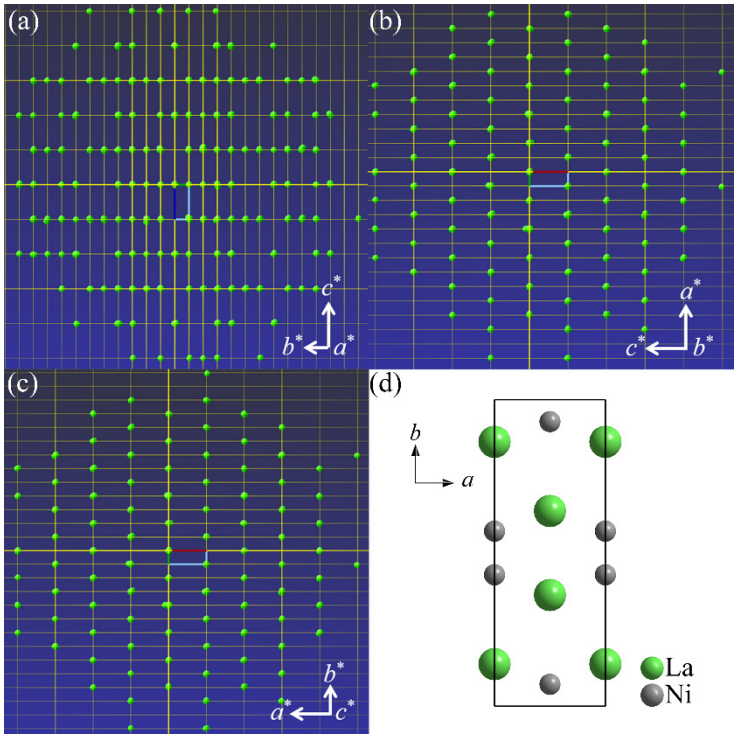

Figure S2. Reciprocal lattice patterns of the LaNi phase projected in three axes: (a) *a** axis; (b) *b** axis; (c) *c** axis and its crystal structure projected in *c* axis (d).

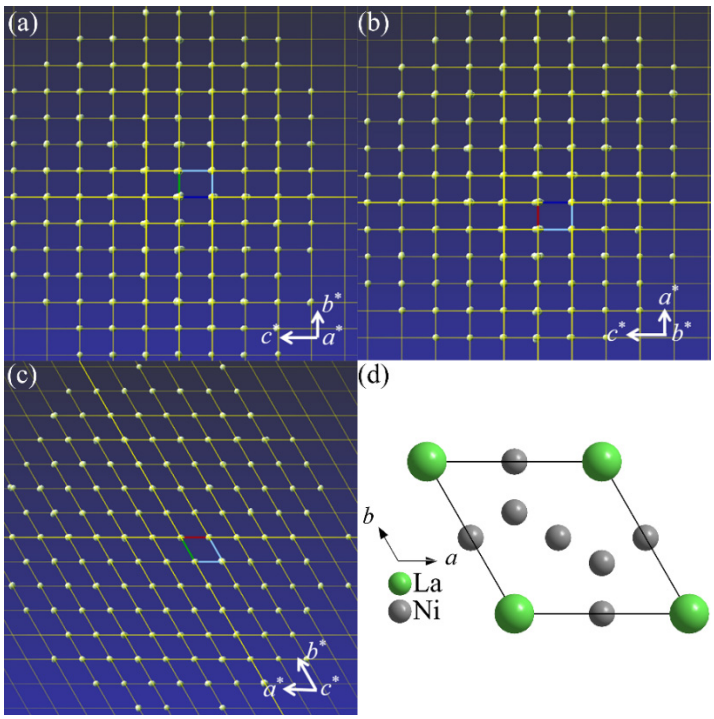

Figure S3. Reciprocal lattice patterns of the $LaNi_5$ phase projected in three axes: (a) *a** axis; (b) *b** axis; (c) *c** axis and its crystal structure projected in *c* axis (d).

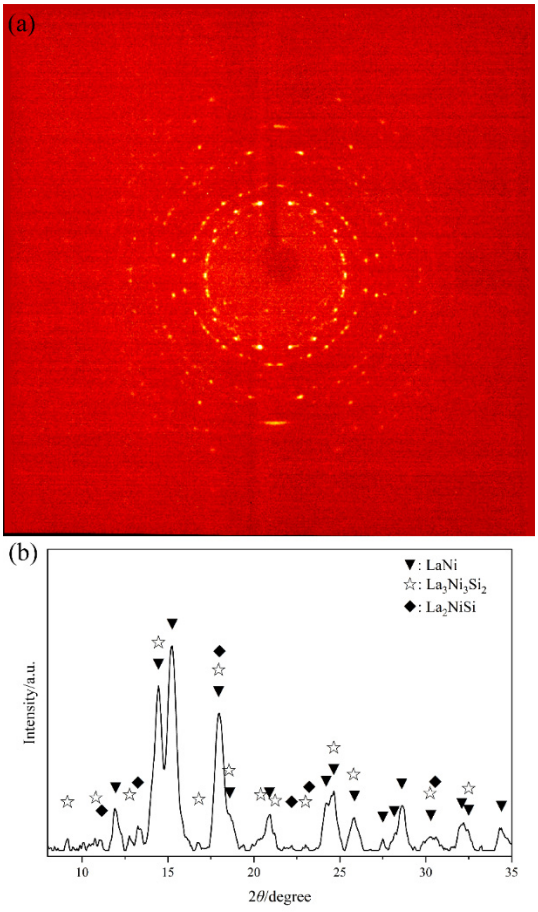

Figure S4. (a) The Phi360 diffraction pattern collected in the process of single crystal testing, (b) the powder diffraction pattern obtained by integrating the Phi360 diffraction pattern.

It can be seen from Figure S4 that the LaNi, $La_3Ni_3Si_2$ and La_2NiSi phases are the dominant phases and there are also few weak peaks which do not belong to phases that may attribute to tiny crystalline phases.

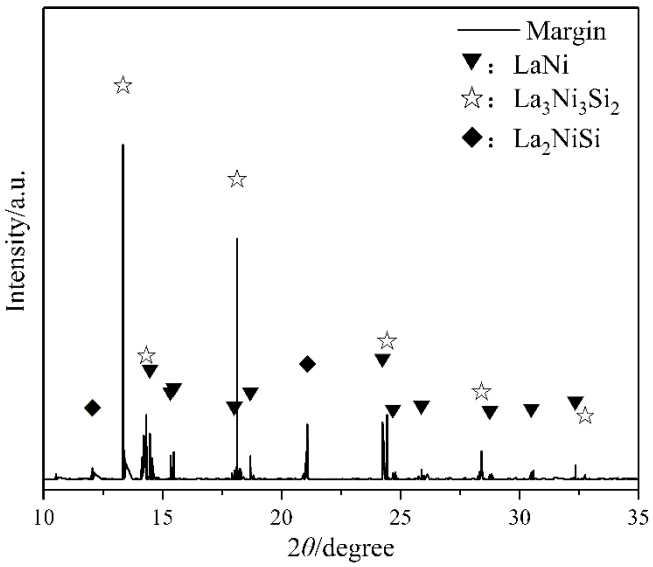

Figure S5. Powder diffraction pattern of the remaining 1094 diffraction points (margin).

From the main text we know that the remaining 1094 diffraction points (margin) cannot be indexed. To investigate the phase to which these remaining diffraction points may belong, we utilized APEX3 software to export these points as p4p file. Subsequently, we obtained the diffraction diagram shown in Figure S5 after processing. It can be observed that the diffraction peaks of these remaining points are highly consistent with the diffraction peaks of the LaNi phase, $La_3Ni_3Si_2$ phase and La_2NiSi phase. That is to say, the remaining diffraction points belong to the three phases of the particularly small grain size.

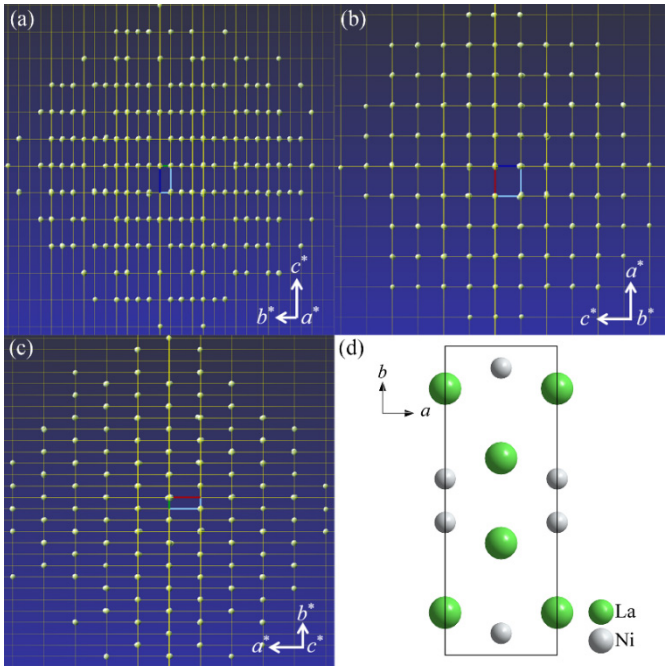

Figure S6. Reciprocal lattice patterns of the LaNi phase projected in three axes: (a) *a** axis; (b) *b** axis; (c) *c** axis and its crystal structure projected in *c* axis (d).

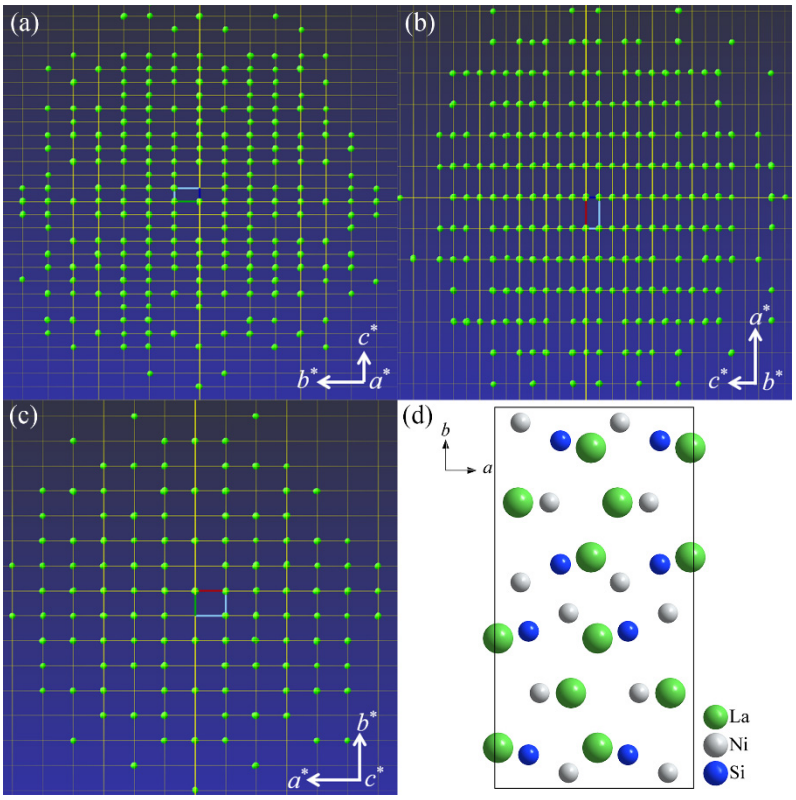

Figure S7. Reciprocal lattice patterns of the $La_3Ni_3Si_2$ phase projected in three axes: (a) a^* axis; (b) b^* axis; (c) c^* axis and its crystal structure projected in c axis (d).

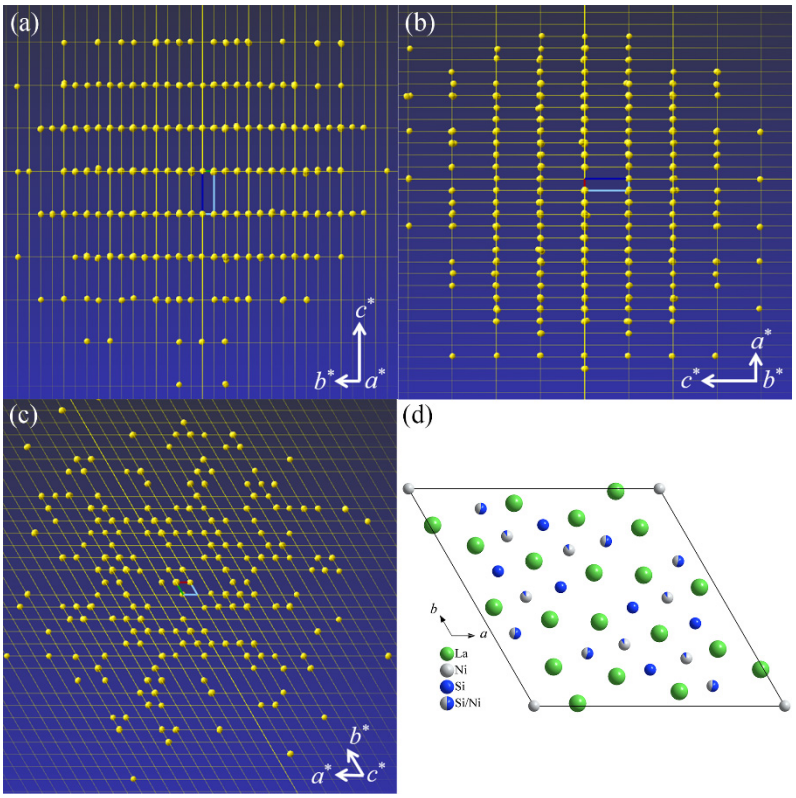

Figure S8. Reciprocal lattice patterns of the La_2NiSi phase projected in three axes: (a) a^* axis; (b) b^* axis; (c) c^* axis and its crystal structure projected in c axis (d).

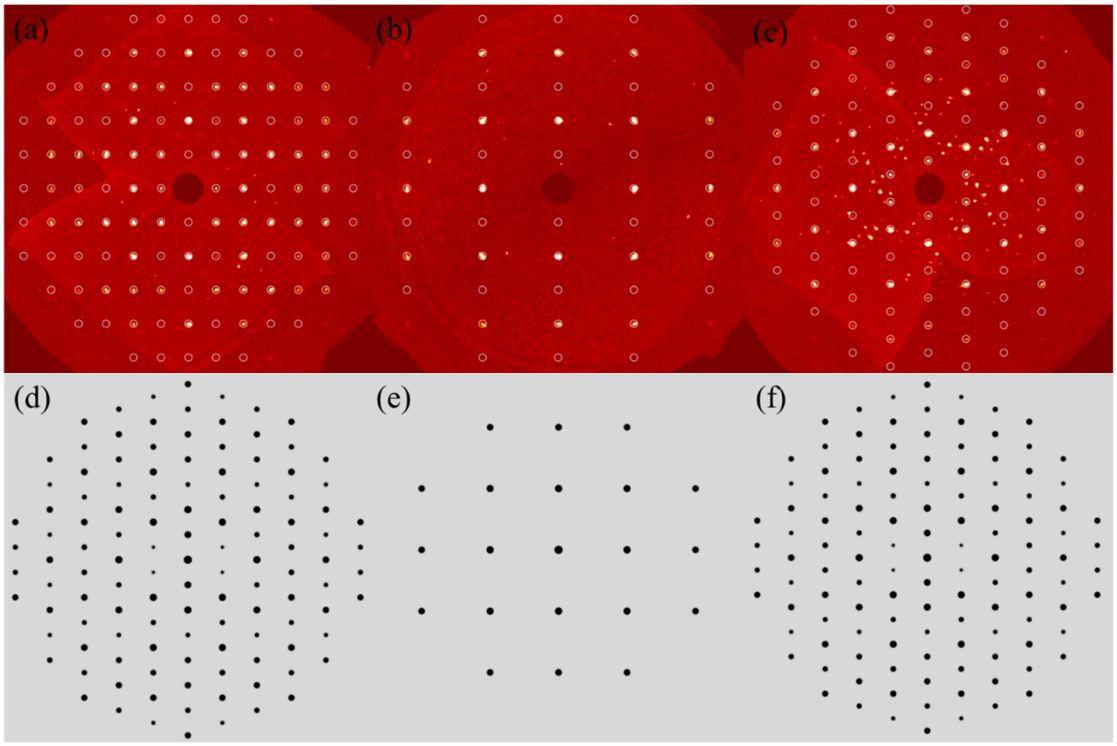

Figure S9. The precession images (a) (0*kl*), (b) (*h*0*l*), (c) (*hk*0) crystal planes of LaNi phase in the SXRD test, LaNi phase simulated diffraction pattern with axes in (d) [100], (e) [010], and (f) [001].

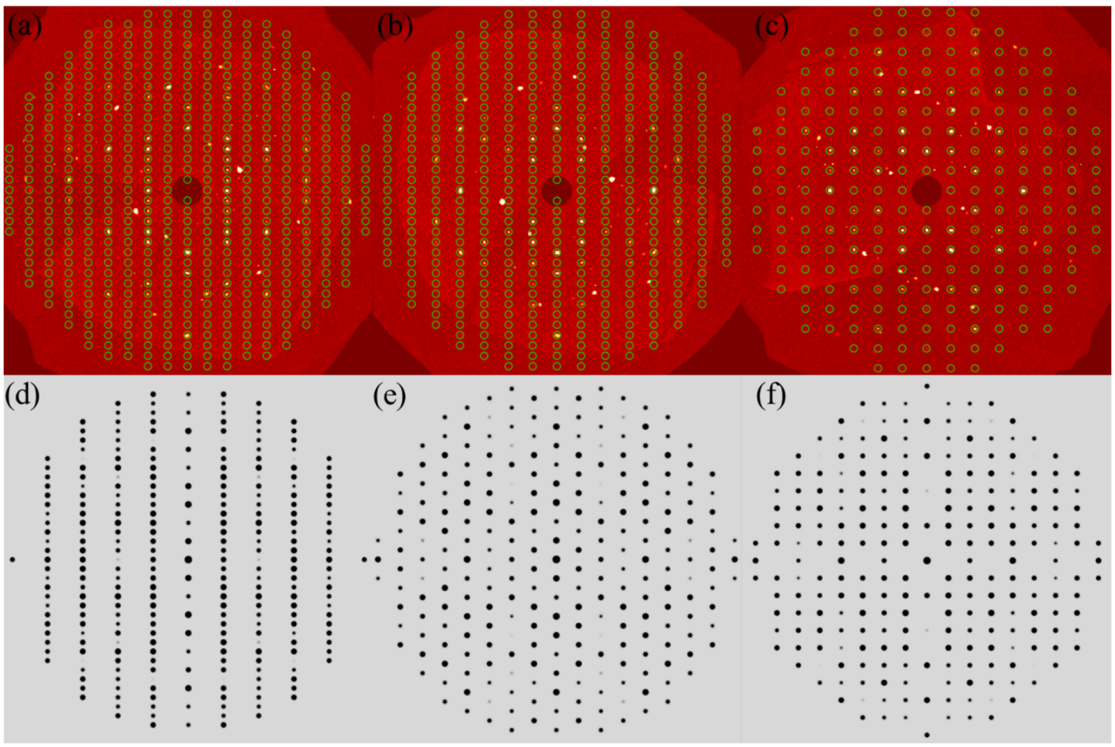

Figure S10. The precession images (a) (0*kl*), (b) (*h*0*l*), (c) (*hk*0) crystal planes of $La_3Ni_3Si_2$ phase in the SXRD test, $La_3Ni_3Si_2$ phase simulated diffraction pattern with axes in (d) [100], (e) [010], and (f) [001].

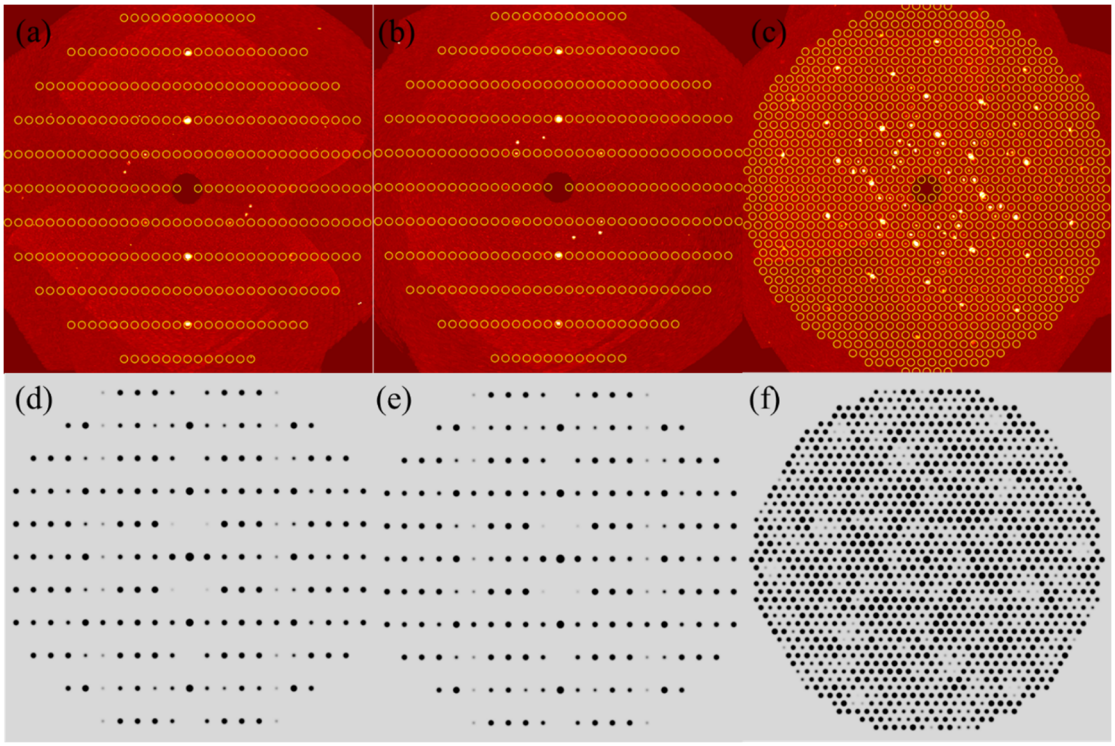

Figure S11. The precession images (a) (0*kl*), (b) (*h*0*l*), (c) (*hk*0) crystal planes of La_2NiSi phase in the SXRD test, La_2NiSi phase simulated diffraction pattern with axes in (d) [100], (e) [010], and (f) [001].

As shown in Figures S9-S11, the results of SXRD experiments correspond to the simulated diffraction patterns one by one, further demonstrating the accuracy of the analytical results of LaNi, $La_3Ni_3Si_2$, and La_2NiSi phases.

In order to determine the single crystal morphology and the proportion of elements in the target sample obtained by sintering, Hitachi S-3400 field emission scanning electron microscope (SEM) was used to observe the morphology of single crystal samples, the elements in the samples were analyzed by energy dispersive X-ray spectroscopy (EDX), which was used in electron microscopy, the types and corresponding contents of the elements were analyzed. Concerning the selected fragment of the single crystal sample, EDX analysis was carried out on four areas and one spot (see Figure S12) and the corresponding results are listed in Table S1. The deviation relative to the results of refinement of chemical composition is probably caused by the tilt of the single crystal surface to the incident beam. In addition, the conductive adhesives and glues may also result in the detected impurity elements of carbon and oxygen. It can be seen that the atomic ratio of La: Ni: Si at Area4 is quite different from other areas. The atomic ratio of Area 4 basically meets the $La_3Ni_3Si_2$ phase, and the atomic ratio of other areas meets the LaNi phase.

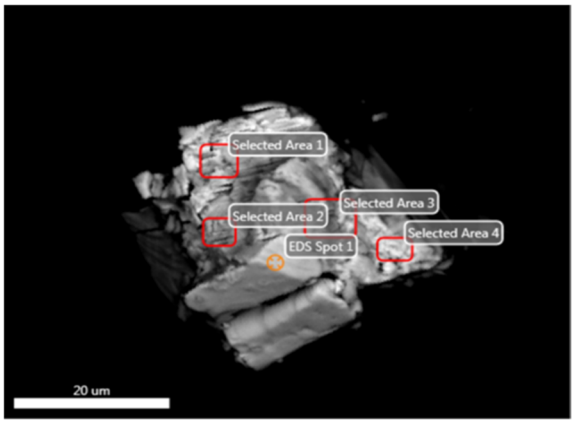

Figure S12. Scanning electron microscope (SEM) micrographs of single crystal sample. EDX analysis was performed for various locations as indicated in Table S1.

Table S1. The EDX results conducted at every scanning location in Figure S12.

	Element	Weight (%)	Atomic (%)	Error (%)	La: Ni : Si
Area1	C	4.94	25.71	9.96	1:1:0.063
	O	4.00	15.62	8.66	
	La	63.70	28.65	2.18	
	Ni	26.56	28.26	3.47	
	Si	0.80	1.77	12.63	
Area2	C	8.45	37.21	9.19	1.1:1:0.01
	O	5.23	17.30	8.67	
	La	62.27	23.71	2.23	
	Ni	23.93	21.56	3.47	
	Si	0.12	0.22	64.33	
Area3	C	5.48	27.72	9.85	1.21:1:0.16
	O	3.84	14.58	8.75	
	La	65.32	28.58	2.13	
	Ni	22.89	23.70	3.54	
	Si	1.70	3.68	9.60	
Spot1	C	3.89	22.17	10.31	1:1:0.023
	O	2.97	12.72	8.85	
	La	65.12	32.08	2.25	
	Ni	27.71	32.29	3.50	
	Si	0.30	0.74	22.22	

	C	5.03	25.58	10.25	
	O	3.53	13.50	8.91	
Area4	La	66.61	29.30	2.14	2.64:1.85:1
	Ni	19.74	20.54	3.66	
	Si	5.09	11.08	8.34	

The chemical compositions were also examined quantitatively by Oxford spectroscopy (EDX) analysis attached to a ZEISS Sigma 300 field emission SEM for the purpose of guiding the crystal structure refinement for the same sample from a different perspective. The examined areas are designated in Fig. S13, and the corresponding results are listed in Table S2. The deviation relative to the results of refinement of chemical composition is probably caused by the tilt of the single crystal surface to the incident beam. For ease of reading, the atomic ratio of La: Ni: Si was calculated and shown in the last column of Table S2. In Table S2, the chemical compositions of Area 3 is in good agreement with La_2NiSi phase. In conclusion, two EDX tests of this single crystal sample indicate that the sample consists of LaNi, $La_3Ni_3Si_2$, and La_2NiSi, showing three-phase coexistence.

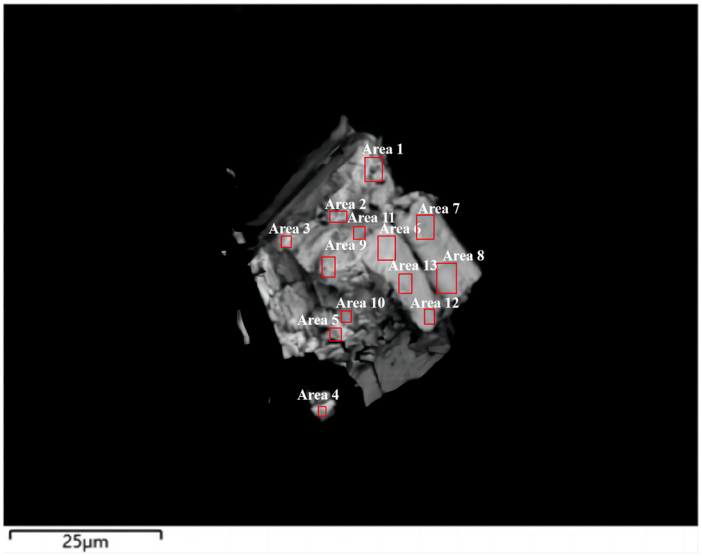

Figure S13. Scanning electron microscope (SEM) micrographs of single crystal sample. EDX analysis was performed for various locations as indicated in Table S1.

Table S2. The EDX results conducted at every scanning location in Figure S13.

	La	Ni	Si	La: Ni: Si Atomic(%)
Area 1	55.2	31.9	12.9	4.28: 2.47: 1
Area 2	57.4	35.3	7.3	7.86: 4.83: 1
Area 3	53.6	23.4	23.1	2.29: 1: 1
Area 4	50.5	18.1	31.4	2.79: 1:1 .73
Area 5	53.6	44.1	2.3	1.22: 1: 0.052
Area 6	51.3	47.1	1.7	1.09: 1: 0.036
Area 7	51.5	46.5	2.0	1.11: 1: 0.043
Area 8	53.7	44.1	2.2	1.22: 1: 0.05
Area 9	52.7	44.4	2.9	1.19: 1: 0.065

Area 10	52.9	45.7	1.3	1.16: 1: 0.028
Area 11	53.7	45.0	1.3	1.19: 1: 0.029
Area 12	51.7	46.5	1.8	1.11: 1: 0.038
Area 13	51.6	46.5	1.9	1.11: 1: 0.041

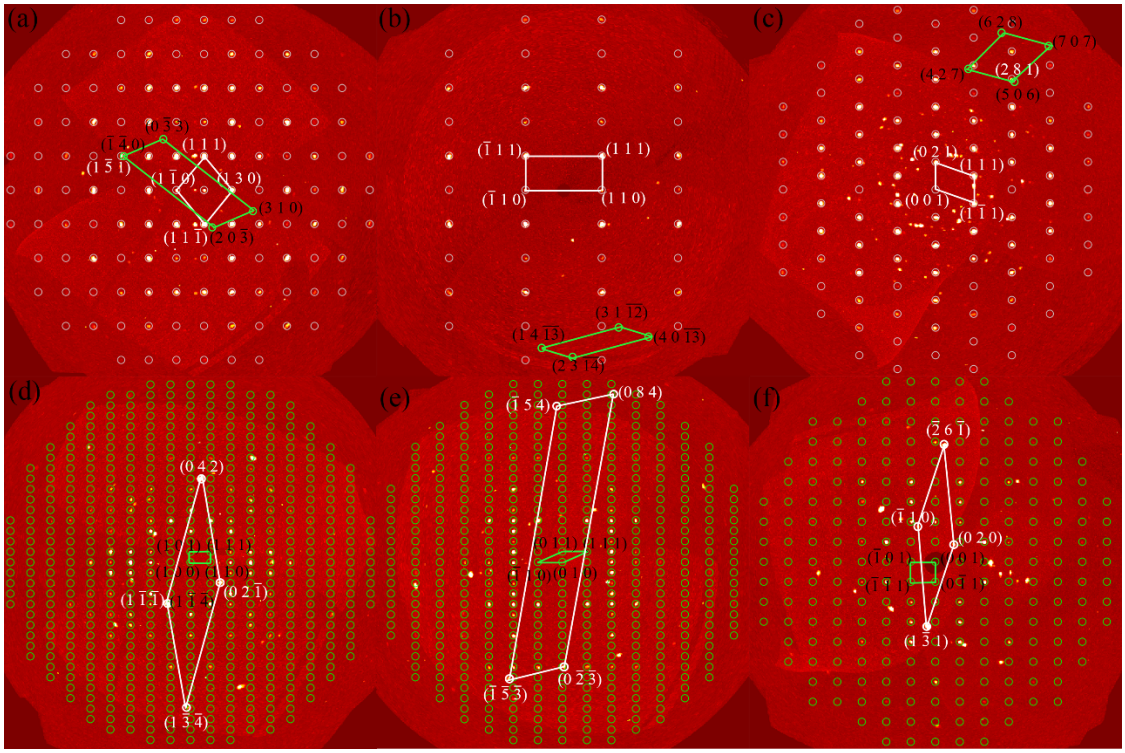

Figure S14. The precession images: (a) LaNi (1*kl*), (b) LaNi (*h*1*l*), (c) LaNi (*hk*1), (d) $La_3Ni_3Si_2$ (1*kl*), (e) $La_3Ni_3Si_2$ (*h*1*l*), (f) $La_3Ni_3Si_2$ (*hk*1).

Figure S14 (a), (b) and (c) represent the precession images of the (1*kl*), (*h*1*l*) and (*hk*1) planes from the LaNi phase while the Figure S14 (d), (e) and (f) represent the precession images of the (1*kl*), (*h*1*l*) and (*hk*1) planes from the $La_3Ni_3Si_2$ phase. In Figure S14 (a), (b) and (c) the precession images are constructed with a thickness of 0.01 $Å^{-1}$ and a resolution of 0.80 Å. While in Figure S14 (d), (e) and (f) the precession images are constructed with a thickness of 0.05 $Å^{-1}$ and a resolution of 0.80 Å. In Figure S14, the white and green circle represents the crystal planes of the LaNi phase and the $La_3Ni_3Si_2$ phase, respectively. Figures S15 and Figure S16 use the same Settings as Figure S14. We can find three kinds of crystal plane parallel relationships in Figure S14 (a), (c), (d). They are $(1\bar{5}1)$ LaNi//$(\bar{1}\bar{5}0)$ $La_3Ni_3Si_2$, (281) LaNi//(506) $La_3Ni_3Si_2$, $(1\bar{1}\bar{1})$ LaNi//$(1\bar{1}\bar{4})$ $La_3Ni_3Si_2$.

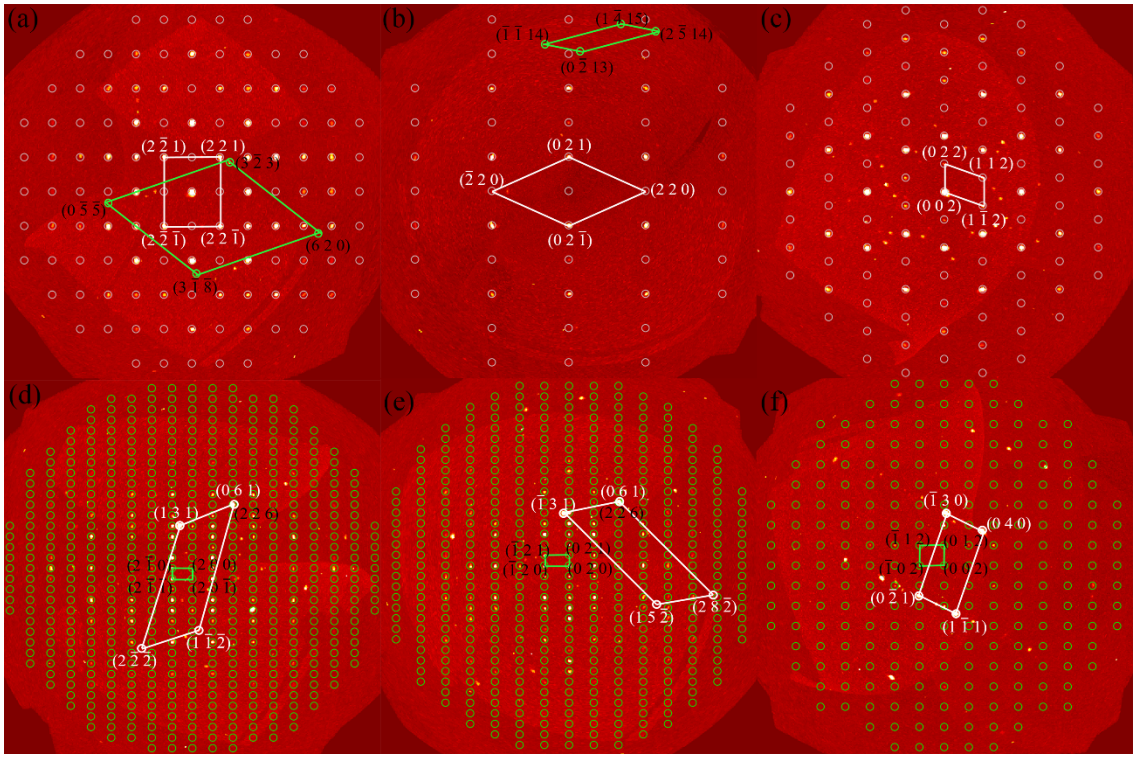

Figure S15. The precession images: (a) LaNi (2*kl*), (b) LaNi (*h*2*l*), (c) LaNi (*hk*2), (d) $La_3Ni_3Si_2$ (2*kl*), (e) $La_3Ni_3Si_2$ (*h*2*l*), (f) $La_3Ni_3Si_2$ (*hk*2).

Figure S15 (d), (e) show same kinds of crystal plane parallel relationships. They are (061) LaNi//(226) $La_3Ni_3Si_2$.

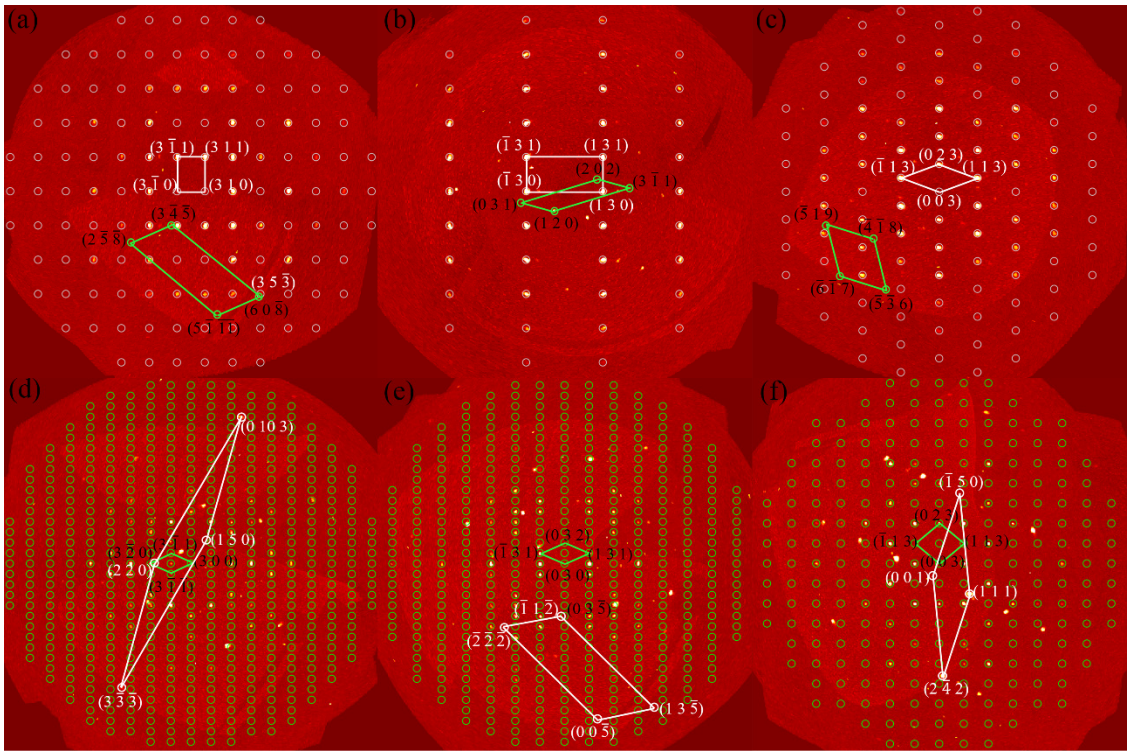

Figure S16. The precession images: (a) LaNi (3*kl*), (b) LaNi (*h*3*l*), (c) LaNi (*hk*3), (d) $La_3Ni_3Si_2$ (3*kl*), (e) $La_3Ni_3Si_2$ (*h*3*l*), (f) $La_3Ni_3Si_2$ (*hk*3).

Figure S16 (a), (d) and (e) show three kinds of crystal plane parallel relationships. They are $(35\bar{3})$ LaNi//$(60\bar{8})$ $La_3Ni_3Si_2$, (220) LaNi//$(3\bar{2}0)$ $La_3Ni_3Si_2$, $(\bar{1}1\bar{2})$ LaNi//$(03\bar{5})$ $La_3Ni_3Si_2$.

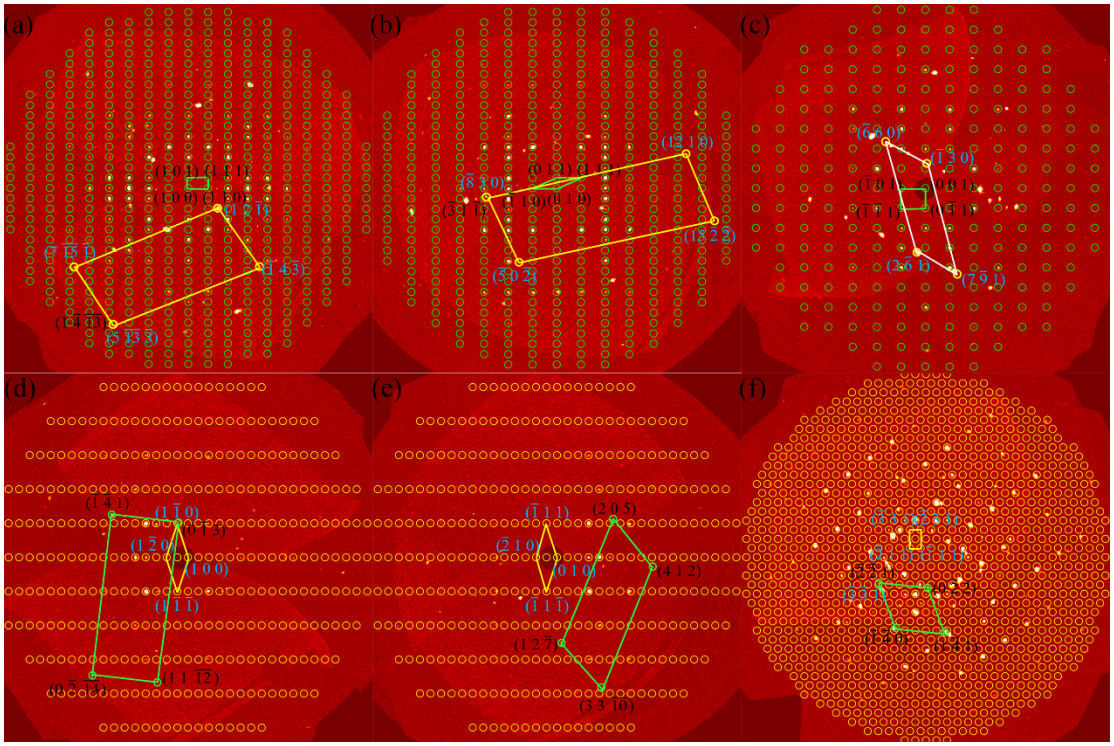

Figure S17. The precession images: (a) $La_3Ni_3Si_2$ (1*kl*), (b) $La_3Ni_3Si_2$ (*h*1*l*), (c) $La_3Ni_3Si_2$ (*hk*1), (d) La_2NiSi (1*kl*), (e) La_2NiSi (*h*1*l*), (f) La_2NiSi (*hk*1).

Figure S17 (a), (b) and (c) represent the precession images of the (1*kl*), (*h*1*l*) and (*hk*1) planes from the $La_3Ni_3Si_2$ phase while the Figure S17 (d), (e) and (f) represent the precession images of the (1*kl*), (*h*1*l*) and (*hk*1) planes from the La_2NiSi phase. In Figure S17 (a), (b) and (c) the precession images are constructed with a thickness of 0.01 $Å^{-1}$ and a resolution of 0.80 Å. While in Figure S17 (d), (e) and (f) the precession images are constructed with a thickness of 0.03 $Å^{-1}$ and a resolution of 0.80 Å. In Figure S17, the green and yellow circle represents the crystal planes of the $La_3Ni_3Si_2$ phase and the La_2NiSi phase, respectively. Figure S18 and Figure S19 use the same Settings as Figure S17. We can find four kinds of crystal plane parallel relationships in Figure S17 (a), (b), (d) and (f). They are $(1\bar{4}\bar{1}3)$ $La_3Ni_3Si_2$//$(5\bar{1}\bar{3}3)$ La_2NiSi, $(\bar{3}1\bar{1})$ $La_3Ni_3Si_2$//(506) La_2NiSi, $(0\bar{1}3)$ $La_3Ni_3Si_2$//$(1\bar{1}0)$ La_2NiSi, $(\bar{2}\bar{2}1)$ $La_3Ni_3Si_2$//$(\bar{3}\bar{3}1)$ La_2NiSi.

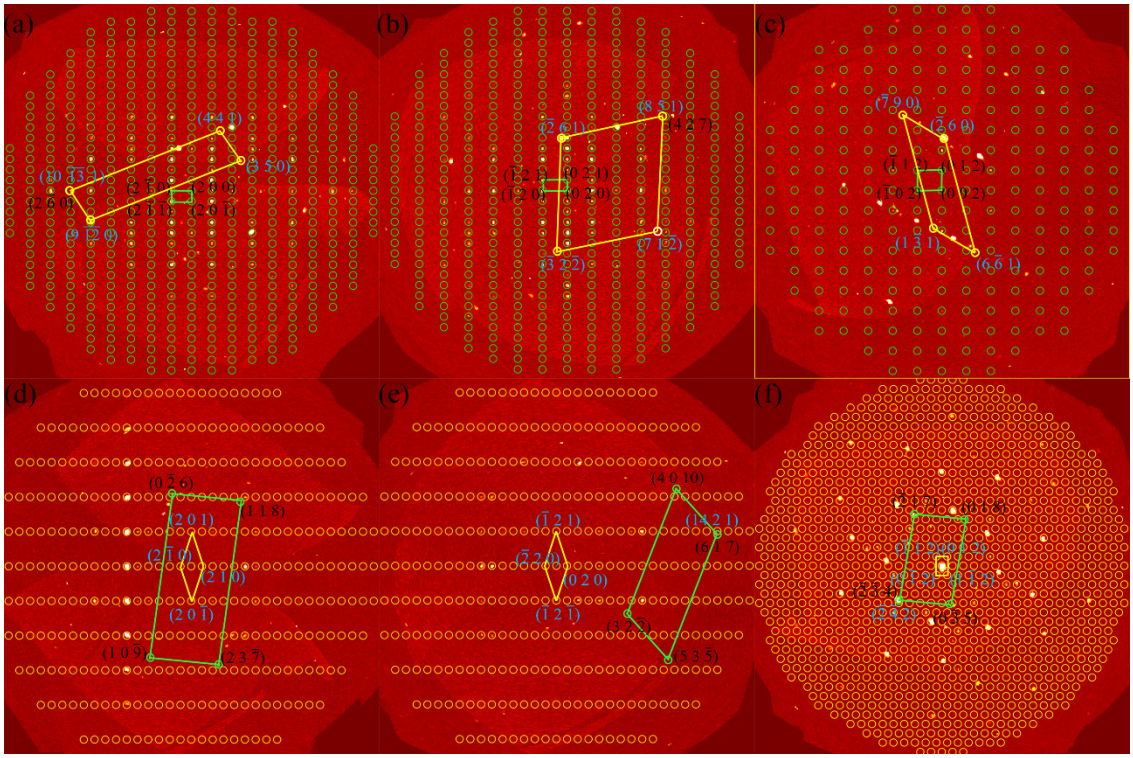

Figure S18. The precession images: (a) $La_3Ni_3Si_2$ (2*kl*), (b) $La_3Ni_3Si_2$ (*h*2*l*), (c) $La_3Ni_3Si_2$ (*hk*2), (d) La_2NiSi (2*kl*), (e) La_2NiSi (*h*2*l*), (f) La_2NiSi (*hk*2).

Figure S18 (a), (b), (e) and (f) show four kinds of crystal plane parallel relationships. They are $(2\bar{6}0)$ $La_3Ni_3Si_2$//$(10\bar{1}\bar{3}1)$ La_2NiSi, (427) $La_3Ni_3Si_2$//(851) La_2NiSi, (617) $La_3Ni_3Si_2$//(14 2 1) La_2NiSi, $(\bar{2}\bar{3}4)$ $La_3Ni_3Si_2$//$(\bar{2}\bar{4}2)$ La_2NiSi.

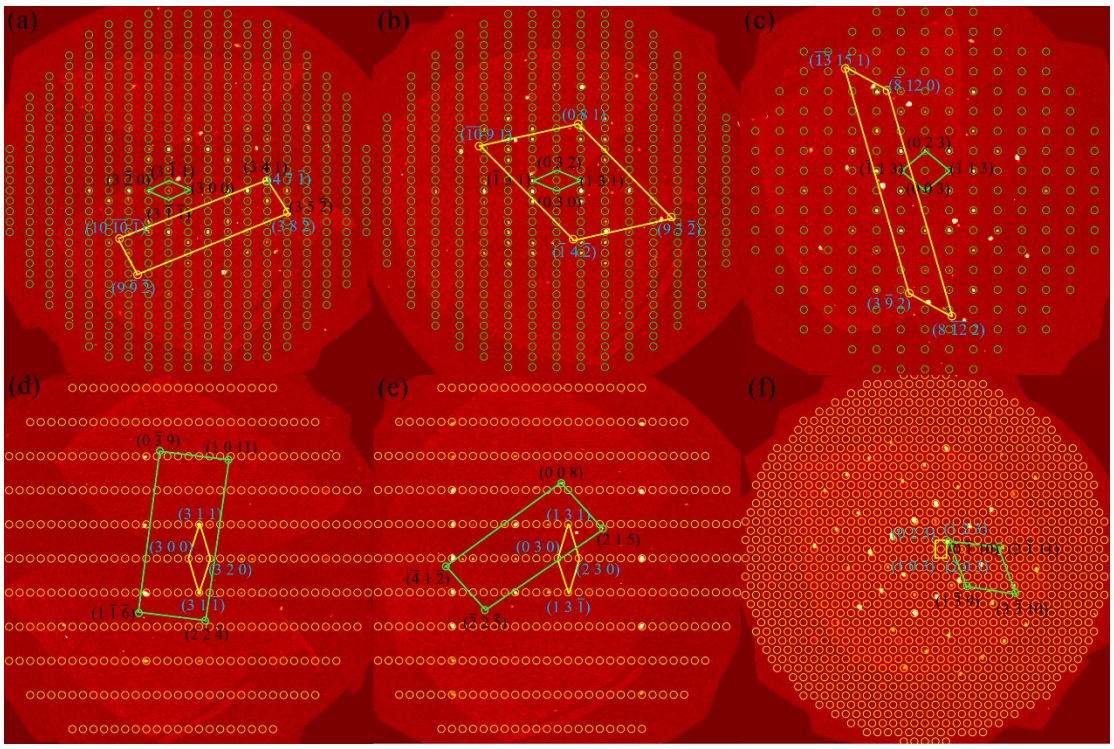

Figure S19. The precession images: (a) $La_3Ni_3Si_2$ (3*kl*), (b) $La_3Ni_3Si_2$ (*h*3*l*), (c) $La_3Ni_3Si_2$ (*hk*3), (d) La_2NiSi (3*kl*), (e) La_2NiSi (*h*3*l*), (f) La_2NiSi (*hk*3).

Figure S19 (a), (f) show three kinds of crystal plane parallel relationships. They are (341) $La_3Ni_3Si_2$//(47$\bar{1}$) La_2NiSi, (35$\bar{2}$) $La_3Ni_3Si_2$//(38$\bar{2}$) La_2NiSi, (0$\bar{1}$10) $La_3Ni_3Si_2$//(123) La_2NiSi.

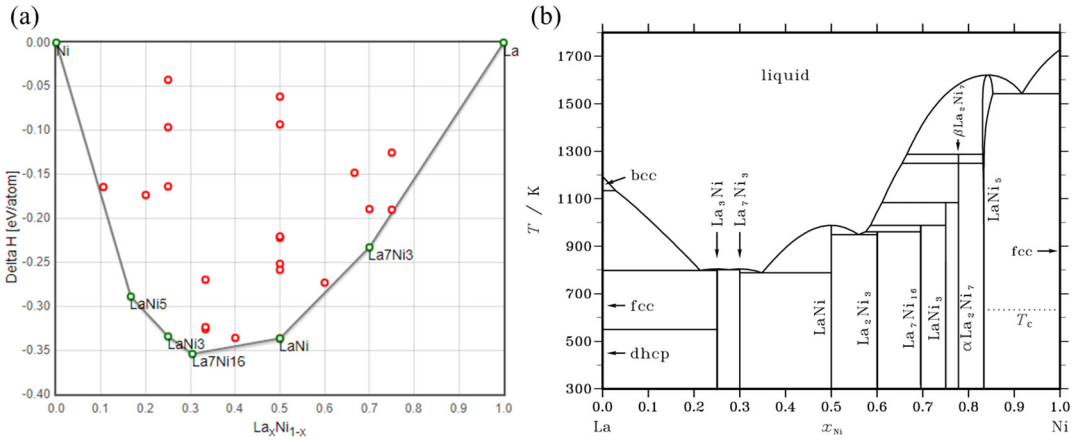

Figure S20. (a)La-Ni binary convex hull, (b) La-Ni binary phase diagram.

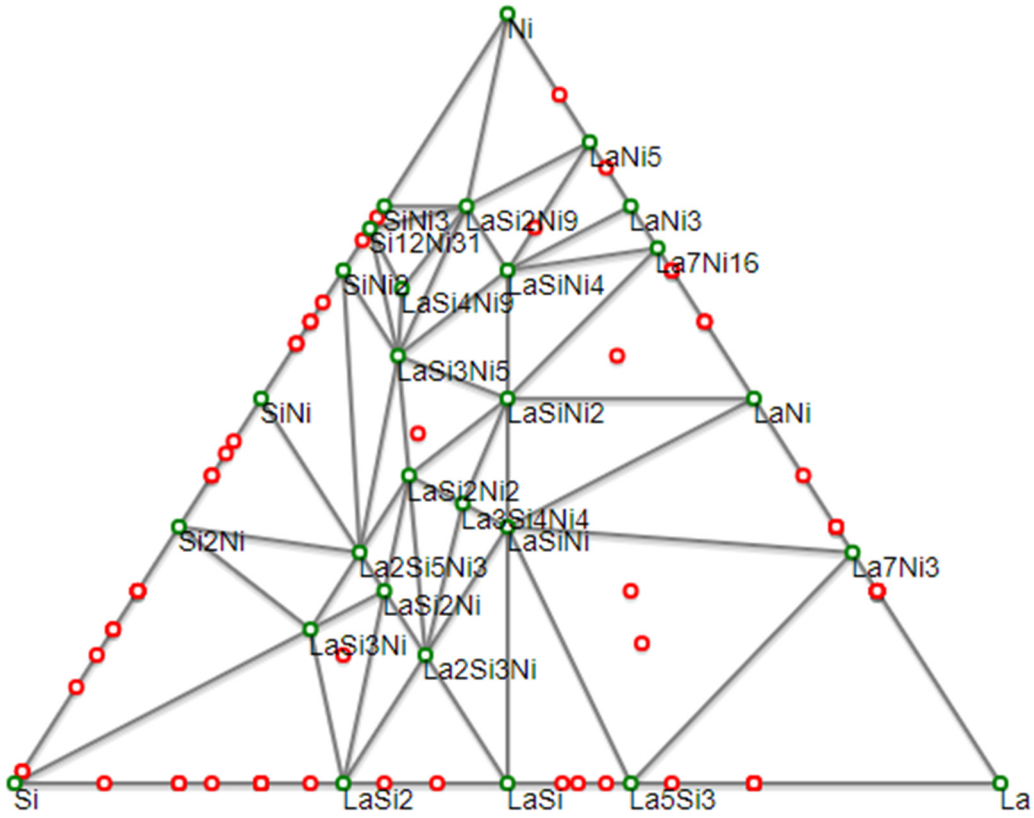

Figure S21. La-Ni-Si ternary phase diagram.

Table S3. Crystallographic and experimental data of $La_3Ni_3Si_2$ phase in another sample.

Chemical formula	**$La_3Ni_3Si_2$**
a, *b*, *c* /Å	7.4763(4), 14.2768(7), 6.1190(3)
α, *β*, *γ* /°	90, 90, 90
V /Å^3	653.13(6)
Z	8

Space group	*Pnma*
Crystal system	Orthorhombic
Diffractometer	Bruker D8 Venture Photon 100 COMS
Monochromator	Graphite
T_{meas} /K	300(2)
Radiation	Mo-Kα, λ = 0.71073 (Å)
Scan mode	φ and ω scan
Time per step /s	3
Absorption correction	Multi-scan
F(000)	1132
θ range /°	4.53 ~ 30.56
μ /mm^{-1}	27.88
No. measured reflections	18527
No. unique reflections	603
No. observed reflections (I > 2σ(I))	560
No. reflections used in refinement	603
No. parameters used in refinement	40
Reflection range	$-8 \le h \le 8$, $-16 \le k \le 16$, $-7 \le l \le 7$
R_{int}	0.0488
R(σ)	0.0129
Final R indices (Fobs > 4σ(Fobs))	R_1 = 0.0222, ωR_2 = 0.0496
R indices (all data)	R_1 = 0.0253, ωR_2 = 0.0496
Goodness of fit	1.393

Table S4. Fractional atomic coordinates and equivalent isotropic displacement parameters (Å^2) of $La_3Ni_3Si_2$ phase in another sample.

Label	**Site**	***x***	***y***	***z***	**Occ.**	**U_{eq}**
La1	8*d*	0.01669 (5)	0.60648 (3)	0.36061 (6)	1	0.00694(15)
La2	4c	0.61643 (7)	0.250000	0.37441 (9)	1	0.00711(17)
Ni1	8*d*	0.12935(11)	0.45976 (6)	0.10093(13)	1	0.0064 (2)
Ni2	4*c*	0.27438(17)	0.250000	0.5629 (2)	1	0.0121 (3)
Si1	8*d*	0.3300 (2)	0.41295(14)	0.3636 (3)	1	0.0060 (4)